



Thermomechanical and damage characterisation of short glass fibre reinforced polyamide 6 and impact-modified polyamide 6 composites

Peihao Song^{a,b}, Akash R. Trivedi^{a,b}, David J. Chapman^{a,b}, Aaron Graham^{a,b}, Nicholas Hawkins^a, Bratislav Lukić^{c,d}, Alexander Rack^c, Clive R. Siviour^{a,*}

^a Department of Engineering Science, University of Oxford, Parks Road, OX1 3PJ, UK

^b DPI, P.O. Box 902, 5600 AX Eindhoven, the Netherlands

^c ESRF the European Synchrotron, CS 40220, F-38043 Grenoble Cedex 9, France

^d Henry Royce Institute for Advanced Materials, Department of Materials, The University of Manchester, Manchester, M13 9PL, UK

ARTICLE INFO

Handling Editor: Prof. Ole Thomsen

Keywords:

Polyamide 6 composites

Impact modifier

Rate- and temperature-dependence responses

High speed imaging

Adiabatic shear bands

ABSTRACT

Polyamide 6 and its composites are widely used in engineering applications that are exposed to high strain rate deformation. This paper investigates the thermomechanical properties of two polyamide 6 composites, both reinforced with 30 wt% short glass fibres, and one of which additionally contains an impact modifier, to provide an understanding of the mechanical response over a wide range of strain rates and temperatures. Compression experiments were performed at rates between 2 and 3000 s⁻¹, with high speed optical and infrared cameras to aid interpretation of the rate-dependent failure arising from the formation of adiabatic shear bands. Further high strain rate experiments were performed with ultra-fast X-ray phase-contrast imaging to provide in-situ internal damage evaluation. These data will improve the utilization of these composites and aid in development of advanced thermomechanical models.

1. Introduction

Polyamide 6 (PA6) is a semi-crystalline thermoplastic polymer with good mechanical properties [1] that enable it to be employed in many engineering applications [2]. In common with other polymers, it is often used as a matrix material for short-fibre composites (SFRCs), which have enhanced mechanical performance over pure polymer material. Whilst there is significant demand for SFRCs, for example in the automotive industry [3,4], there is a lack of experimental data on their properties, especially under high strain rate loading of the type that might be experienced in automotive or sports applications.

The thermomechanical properties of PA6 resin have been extensively investigated experimentally [1,5–7] and numerically [8]. However, such a wide dataset for PA6 composites has not been established. Tensile test data in the literature show the importance of factors such as fibre flow orientation [4,9], fibre volume fraction [10,11], fibre type [12], fibre length distribution [11], fibre-matrix interface [13] and temperature [4] on the mechanical properties, but there are few studies on the rate dependence extending to high strain rates for polyamide composites [14–17].

Measurements of high strain rate properties of materials are typically performed using hydraulic test machines (1–100 s⁻¹) and Split Hopkinson Pressure Bar (SHPB, above 1000 s⁻¹) [18,19]. A critical feature of inelastic deformation under high rate loading is the temperature rise, caused by the production of heat from inelastic work [20]. Under dynamic loading, there is not sufficient time for the heat to be dissipated, the experiment is adiabatic or near adiabatic, and the subsequent temperature rise can affect the thermomechanical response, especially for polymeric materials [21]. As the temperature rises, the material experiences a notable reduction in strength, leading to unstable deformation, which may cause the development of adiabatic shear bands [22]. It is challenging to quantify the temperature during high-rate tests: thermocouples do not have the required response time, and single point IR detectors are insufficient to understand heterogeneous composite materials, whilst high speed thermal imaging cameras can still only take images at speeds up to 100,000 frames per second. Recently, Song et al. [1,23] developed a method for high-speed IR imaging in which the trigger time is shifted between experiments to construct ‘continuous’ high quality thermal images during SHPB experiments. This method successfully captured the adiabatic shear band formation in a short glass

* Corresponding author.

E-mail address: clive.siviour@eng.ox.ac.uk (C.R. Siviour).

<https://doi.org/10.1016/j.compositesb.2024.111767>

Received 29 May 2024; Received in revised form 17 July 2024; Accepted 13 August 2024

Available online 18 August 2024

1359-8368/© 2024 The Authors. Published by Elsevier Ltd. This is an open access article under the CC BY license (<http://creativecommons.org/licenses/by/4.0/>).

fibre reinforced polycarbonate composite during the 400 μs test duration [23]; this method was applied to PA6 resin [1].

The present study investigates the thermomechanical behaviours of injection moulded 30 wt% short glass fibre reinforced PA6 with and without an impact modifier. Frequency sweep dynamic mechanical analysis (DMA) was performed to obtain the time and temperature dependent viscoelastic behaviour. Compression tests were performed from -60 to 200°C at 0.01 s^{-1} strain rate, and from 0.001 to 3000 s^{-1} at room temperature. High speed optical and IR cameras were used at rates from 2 to 3000 s^{-1} to record the deformation and failure processes in the specimens. Furthermore, dynamic compression experiments were performed using an SHPB at the European Synchrotron Radiation Facility (ESRF) to explore internal damage information [24]. Together these give a comprehensive dataset for future development of advanced constitutive model of short fibre reinforced composites.

2. Material information and sample preparation

Injection moulded sheets of 30 wt% short glass fibre reinforced PA composites were provided by DSM Engineering Materials. The materials are branded as Akulon® K224-G6 [25] and K224-PG6 [26], and are named GFPA6 and GFIMPA6 in this work. The PA6 matrix of K224-PG6 is modified by a functionalized thermoplastic polyolefin elastomer impact modifier with dispersed domain sizes in the order of microns (hence IM). This modifier enhances the impact strength and notch sensitivity [27]. More detailed information on the mechanical properties of the two materials is given in Appendix A. The sheets have dimensions of $300 \times 100 \times 2\text{ mm}^3$; the fibre diameter is about $10\text{ }\mu\text{m}$, and the fibre length is between 200 and $400\text{ }\mu\text{m}$. The sheets were delivered in sealed bags marked 'dry as moulded'. Test specimens were cut from these sheets, promptly placed in vacuum-sealed bags, and stored in a freezer to minimize water absorption. Prior to testing, specimens were brought back to room temperature and only then taken out of the vacuum packaging.

All samples were cut from the centre area of the sheets, about $100 \times 100\text{ mm}^2$, where it has been established that the fibre flow orientation is consistent. DMA samples were $60 \times 10 \times 2\text{ mm}^3$ rectangular bars and cut inline with (0°) and parallel to (90°) the fibre flow orientation. Tensile samples were also cut in 0° and 90° directions with the geometry of ISO 527 type 1BA [28]. The gauge length was 30 mm with a $2 \times 5\text{ mm}^2$ cross-section area; the schematic drawing can be found in Ref. [1]. Compression samples were cut from the through-thickness direction with 4 mm diameter and 2 mm thickness: the loading direction was normal to the fibre flow orientation. These specimens were used for all temperature- and rate-dependent compression experiments *except* those in Fig. 10, which reports data from experiments performed in ESRF, where, owing to the imaging setup, the samples were 1 mm in diameter and thickness, and also cut from the through-thickness direction.

3. Experimental procedure

3.1. Dynamic mechanical analysis (DMA)

Our previous research [1] used three-point bend DMA with a 50 mm span to measure viscoelastic properties of PA6 resin. The storage modulus obtained was consistent with tensile test data. Thus, the same method was used in the current research. Isothermal frequency sweeps were conducted at 2°C increments from -90 to 80°C , which covers both the secondary (β)- and glass (α)-transitions of the PA 6 resin, with a 5-min equilibrium time at each step. At each temperature, oscillatory displacement with 0.1% strain amplitude and 125% force track was applied at frequencies of 0.1 , 0.25 , 1 , 2.5 and 10 Hz .

3.2. Mechanical tests

Rate dependent tests were performed using an SHPB system and

hydraulic machine described in Ref. [1]. The input, output and striker and output bars were Ti-6Al-4V rods with 12.7 mm diameter, and lengths shown in Fig. 1. In all rate-dependent tests, petroleum jelly [29] was used as a lubricant to minimize the friction effect [29]. The temperature-dependent compression tests were conducted using a traditional screw-driven machine (Fig. 1(c)) equipped with an environmental chamber. The sample was held for 5 min at the test temperature before each test to ensure thermal equilibrium, moreover, a thermocouple was attached to the loading anvil adjacent to the specimen, and compared to the main thermal chamber thermocouple ensure repeatable thermal conditions. In addition, although not the focus of this research, a small number of tensile tests were performed to enhance the data set of GFPA6 and GFIMPA6. The loading speed was 10 mm/min for all tensile tests.

3.3. Optical imaging

Optical and thermal images were captured using a Photron Fastcam SA-Z high-speed camera and a Telops M3K thermal camera, respectively, using the settings in Table 1. High speed optical and IR imaging were performed separately because of the difficulty of applying both at the same time to the small specimens. However, each test was repeated more than three times to ensure the consistency of test results.

The optical camera used a 200 mm Nikon lens and is capable of recording continuous full-field images during medium and high rate experiments. In the medium rate tests, the camera was synchronized using the loading command signal from the apparatus and a constant light was used; at high strain rates, the gauge on the input bar was used to trigger the camera and a flashlight. The experimental details for the high-speed IR imaging are the same as those used for PA6 resin [1], including the emissivity of 0.965 . The Telops M3K can provide a sufficient frame rate to record continuous full-field thermal images at medium rates, but not in high rate experiments. Thus, the 'shift and reconstruction' method has been developed to obtain 'continuous' thermal images [1], and the results are reproduced in Appendix C as validation for the current work.

The in-situ dynamic measurement on GFPA6 was performed at the ID-19 beamline at ESRF; detailed information on the SHPB system used for this work can be found in Refs. [23,30]. The experimental setup employs an ultra-fast indirect X-ray detector with increased sensitivity to near-ultra violet emission, providing $10\times$ magnification, an approximately $1.28 \times 0.8\text{ mm}^2$ field of view with a pixel size of $3.2\text{ }\mu\text{m}$ and approximately 3 pixels across the $10\text{ }\mu\text{m}$ fibre diameter. X-ray phase contrast (XPCI) techniques [31] were employed to enhance the visualisation of the internal damage process; more experiment details are given in Ref. [23].

4. Results and discussion

4.1. Dynamic mechanical analysis

DMA results from PA 6 resin [1] are shown, along with GFPA6 and GFIMPA6 cut from different orientations, in Fig. 2. The reinforcement increases the stiffness of the materials, in particular in the fibre flow orientation (0°). The data in Fig. 2(a) and (b) show the effect of the low temperature β -transition and high temperature α -transition on the storage and loss moduli. The secondary (β)-transition, has been proven to be strongly associated with the high strain rate performance of polymers [18,19,32], causing an increase in strength at low temperatures or high strain rates.

To predict E' at higher strain rates, time-temperature superposition (TTS) was used to shift the isotherms in Fig. 2(a), results from four samples are shown in Fig. 2(c). The construction of the master curve by TTS is given in Refs. [1,33]; here, the reference temperature is 20°C . To allow easier comparison to the compression data presented later, the master curve is given as a function of strain rate, estimated as [18]:

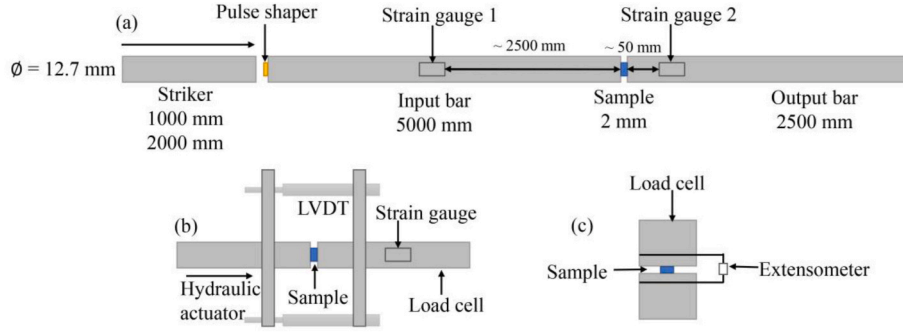


Fig. 1. (a) SHPB for high rate tests (b) Hydraulic machine for medium rate tests (c) Screw-driven machine for quasi-static tests. Reproduced from Ref. [1]. The pulse shaper is a disc of card.

Table 1

Optical and IR camera settings for rate-dependent tests.

Strain rate	Optical camera		IR camera		
	Frame rate (Hz)	Window size (pixel ²)	Frame rate (Hz)	Exposure time (μs)	Window size (pixel ²)
2 to 20 s ⁻¹	3000	1024 × 1024	1000	100	192 × 100
3000 s ⁻¹	100,000	384 × 264	10,000	20	128 × 92

$$\dot{\epsilon} \approx \frac{\Delta \epsilon}{\Delta t} = \frac{\epsilon_0}{1/4f} = 4f\epsilon_0 \quad (1)$$

where, f and ϵ_0 are the applied frequency and strain amplitude in the DMA test. Fig. 2(d) shows the shift factor, $\log(a_T)$ as a function of temperature. The data show that the impact modifier reduces the value of E' between the two transitions and also increases the onset temperature of the β -transition.

4.2. Varying temperature and rate compression tests

All compression specimens were prepared with the loading axis through-thickness: they were subjected to load perpendicular to the direction of fibre flow. Fig. 3(a) and (b) present the compressive

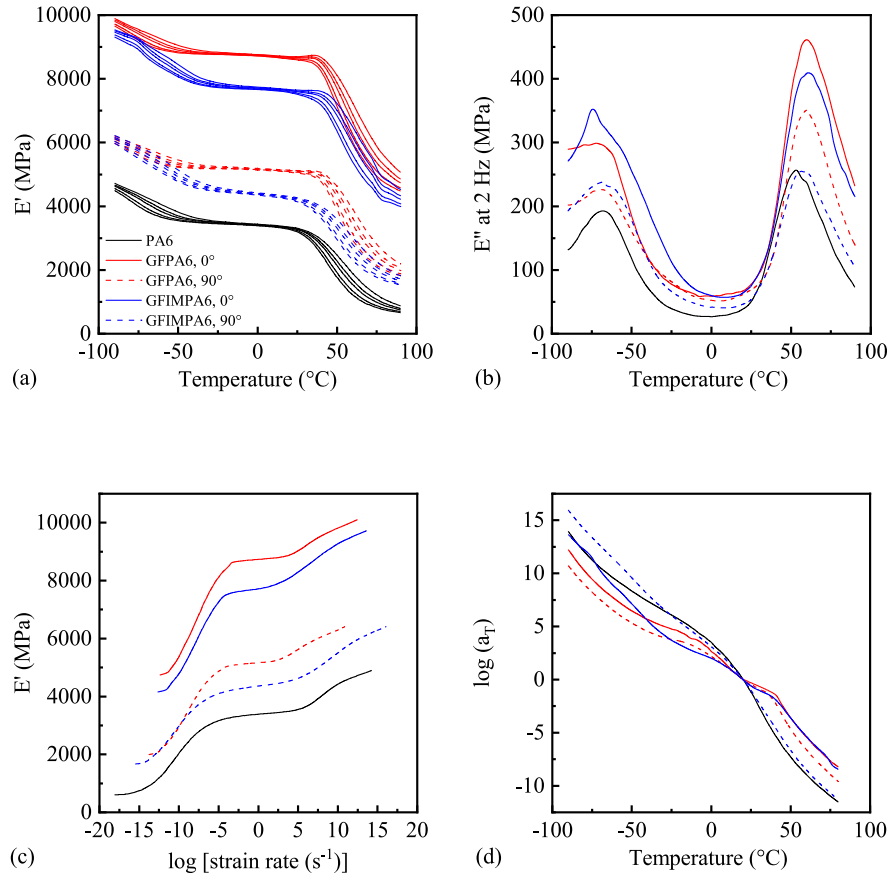


Fig. 2. (a) Storage modulus (E') versus temperature at 0.1, 0.25, 1 2.5 and 10 Hz (b) Loss modulus (E'') versus temperature at 2.5 Hz (c) master curve of E' versus logarithm strain rate (d) Shift factor [$\log(a_T)$] versus temperature. PA6 data is from Ref. [1].

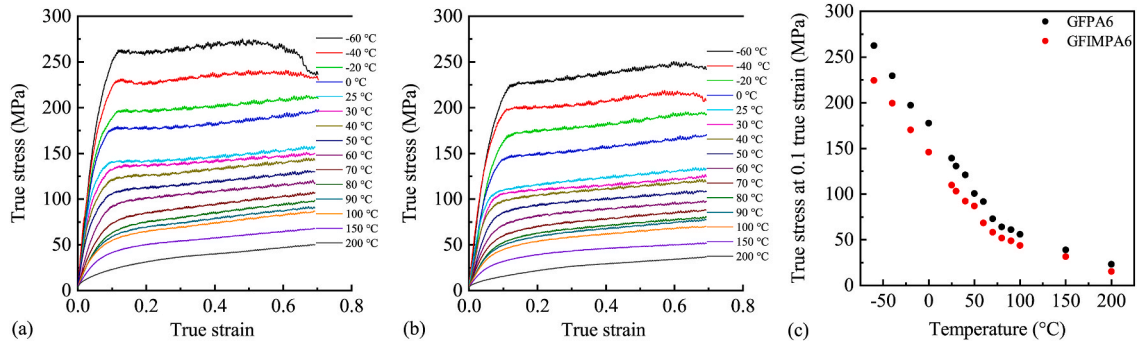


Fig. 3. Temperature-dependent compression tests at 0.01 s^{-1} for (a) GFPA6 and (b) GFIMPA6; (c) True stress at 0.1 true strain for GFPA6 and GFIMPA6.

response of the GFPA6 and GFIMPA6 at a constant true strain rate of 0.01 s^{-1} and temperatures from -60 to 200°C , which covered the β - and α -transition of the matrix materials. Three tests were performed at each temperature, data from one test at each temperature are shown here, whilst the full data set will be made available on an online repository. Due to there being no distinguishable peak at yield in these materials, the data were parameterised for comparison by finding the stress at a true strain of 0.1, Fig. 3(b). GFPA6 shows a higher stress than GFIMPA6 at any given temperature. It is worth noting that the test at -60°C for GFPA6 shows a stress drop at large strain owing to fracture; this is not observed in the GFIMPA6.

Fig. 4(a) and (b) illustrate the rate-dependent compressive responses of GFPA6 and GFIMPA6. Here, the distinguishable peaks were used as yield stresses in higher strain rate experiments (above 5 s^{-1}), and the stress at 0.1 true strain was defined as yield stresses in quasi-static tests. More detailed information on SHPB data processing is given in Appendix B. For both materials, an increase in strain rate and a decrease in temperature can strengthen the material, meeting the well-known time-temperature equivalence between temperature and strain rate. Moreover, the yield stress demonstrates a bilinear dependence on log strain rate, Fig. 4(c), which is similar to the neat polyamide 6 [1] and attributed to the secondary (β)-transition of the matrix material. Following yield, an apparent stress drop at large strains was observed for both materials at strain rates above 5 s^{-1} , this observation was caused by the crack or failure and confirmed by high speed optical and IR photographs.

4.3. Tensile tests

Fig. 5 shows tensile test results. In the same loading direction, the stiffness and strength of GFPA6 are higher than those of GFIMPA6, which quantitatively agrees with the DMA test results.

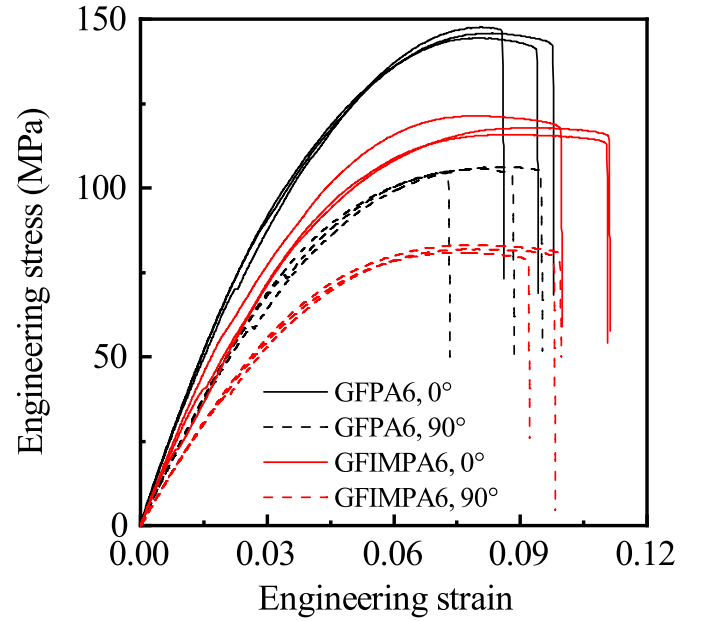


Fig. 5. Engineering stress versus engineering strain curves for GFPA6 and GFIMPA6 in 0° and 90° direction under 10 mm/min tensile loading.

4.4. Photography in rate-dependent tests

4.4.1. Medium rate

Fig. 6(a) shows data from six experiments on each material at a strain rate of about 2.2 s^{-1} : three tests with an optical camera and three with an IR camera. The stress-strain curves for each material are very consistent.

Fig. 6(b) shows stress and temperature data for one test for each

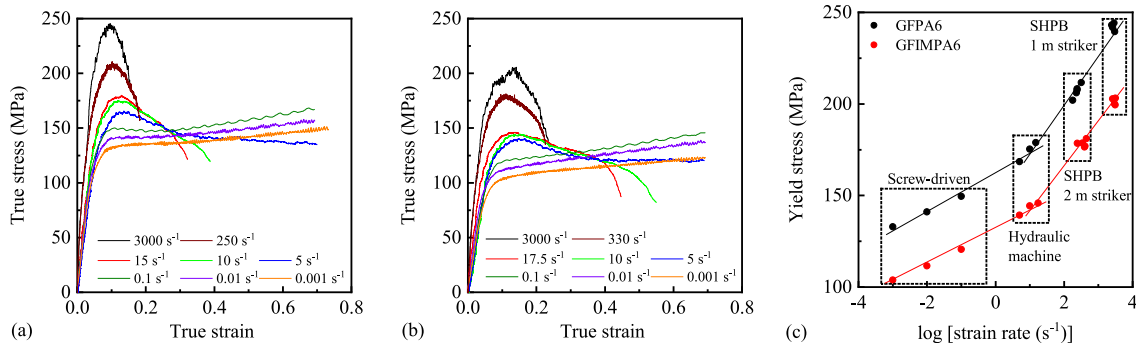


Fig. 4. (a) Rate-dependent compression tests at room temperature for (a) GFPA6 and (b) GFIMPA6; (c) Rate-dependent yield stress for GFPA6 and GFIMPA6.

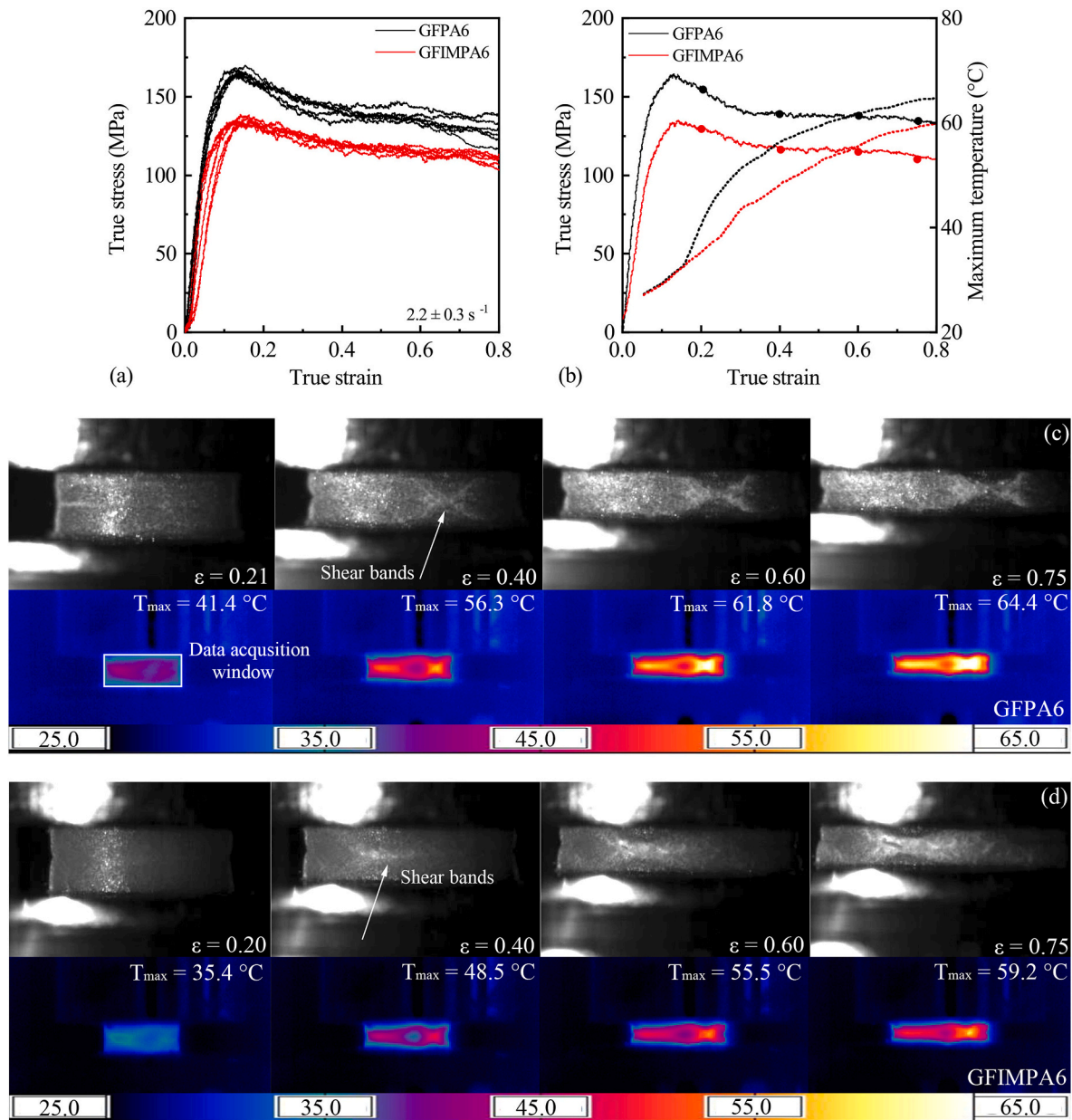


Fig. 6. (a) True stress versus true strain curves for six medium rate tests at approximately 2.2 s^{-1} on two materials; (b) Example of true stress (solid line) and maximum temperature (dotted line) versus true strain for GFPA6 and GFIMPA6; (c) and (d) representative thermal and optical images as functions of strain.

material. Before yield, the maximum temperatures of the two materials are very close. After yield, the maximum temperature in GFPA6 is higher than in GFIMPA6; this is attributed to the higher stress. At the same time, stress localisation was observed in optical images for both materials, and, correspondingly, thermal inhomogeneities were also observed. No obvious fracture was observed at this strain rate (2.2 s^{-1}) for either material at the strains achieved.

Fig. 7(a) presents equivalent data at a strain rate of 17 s^{-1} . Unlike the results at 2.2 s^{-1} , there are evident stress drops for both materials, and these drops occurred at smaller strains for GFPA6 compared to GFIMPA6. Correspondingly, Fig. 7(b) shows a faster temperature rise before the stress drop, after which the temperature remains constant.

Considering Fig. 7(c) and (d) for the GFPA6, at 0.34 true strain, a crack was observed in the optical image, consistent with the increased temperature in the thermal image in Fig. 7(c). For GFIMPA6, the crack occurred at 0.43 strain in the optical image, later than in the GFPA6, and the temperature localisation is less significant.

4.4.2. High rate

Fig. 8(a) presents three stress-strain curves for each of the two materials, optical images were obtained continuously, and a set of these, at strains illustrated in Fig. 8(b) are shown in Fig. 8(c) and (d).

Fig. 8(a) shows that the stress drop for both materials occurs at smaller strains compared to the lower strain rate test in Fig. 7(a). Again, the stress drop in GFPA6 was observed at smaller strains than in GFIMPA6. This is supported by the crack observations in Fig. 8(c) and (d). After the crack forms, the stress drops significantly; these observations are consistent with data obtained at 17 s^{-1} .

High speed thermal images are reconstructed using five SPHB tests, Fig. 9(a), by shifting the trigger time of the IR camera. The method has been validated using PA6 resin, see Appendix C [1]. Fig. 9(b) combines the maximum temperature versus true strains measured using all images from the five tests for both materials. There are three distinct stages: small temperature rise before yield, dramatic temperature rise, then constant temperature after failure, consistent with the experiments at 17

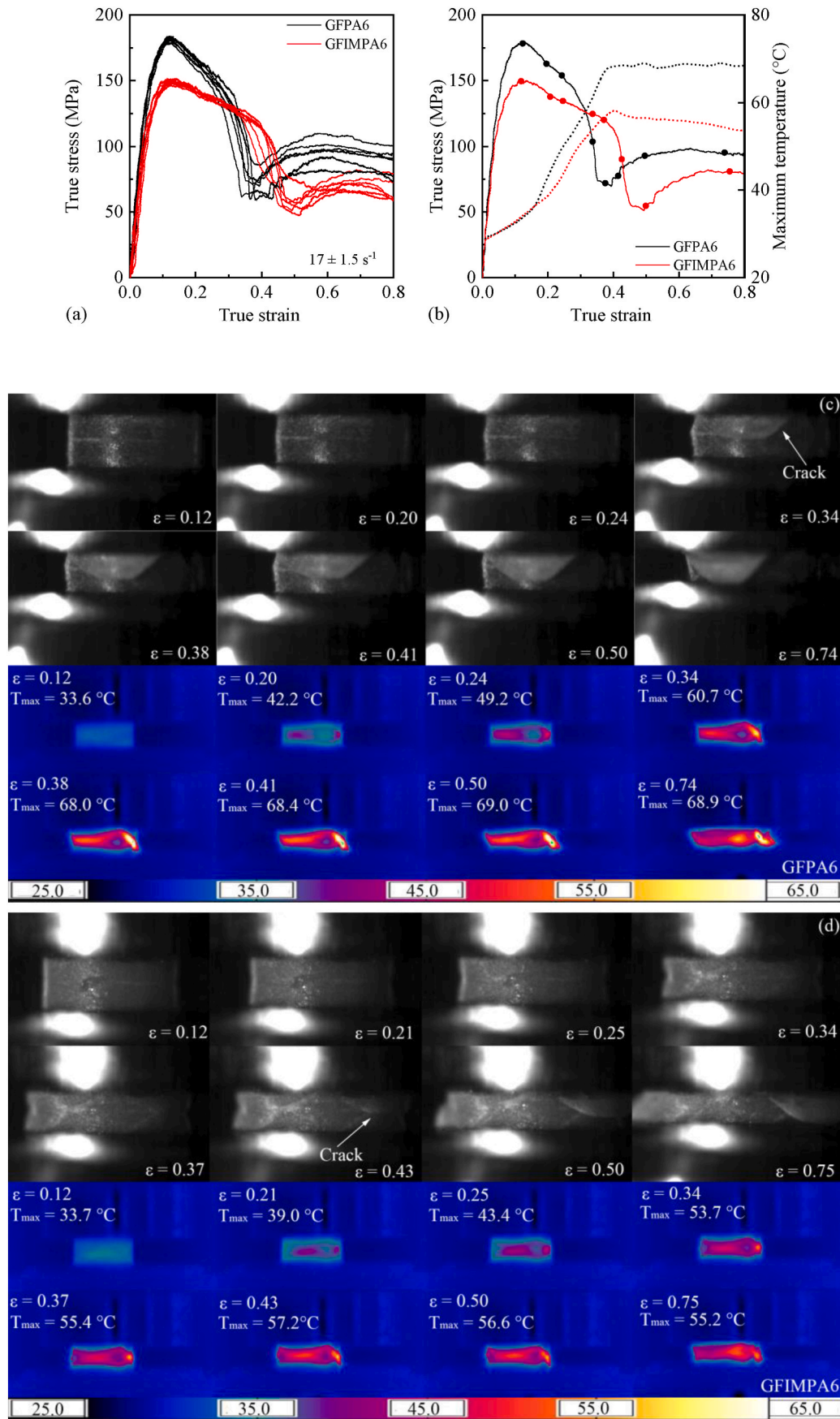


Fig. 7. (a) True stress versus true strain curves for six experiments at about 17 s^{-1} on two materials (b) Example of true stress (solid line) and maximum temperature rise (dotted line) versus true strain for GFPA6 and GFIMPA6; (c) and (d) representative thermal and optical images as functions of strain.

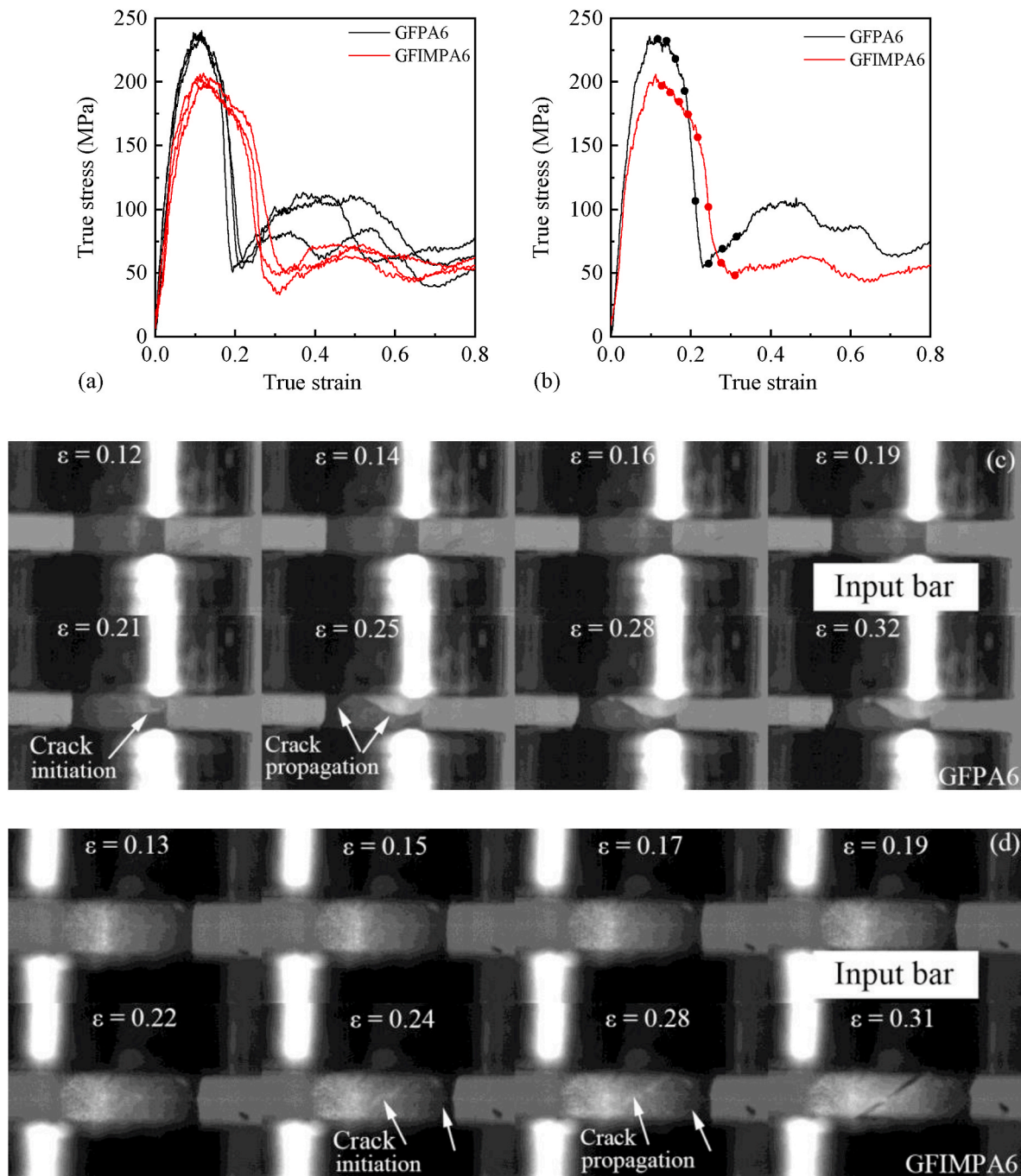


Fig. 8. (a) True stress versus true strain curves for GFPA6 and IMPA6 at about 3000 s^{-1} ; (b) Representative data point selection; (c) and (d) Deformation to failure process of GFPA6 and GFIMPA6 at the data points in (b).

s^{-1} in Fig. 7(b).

Fig. 9(c) and (d) plot representative thermal images for GFPA6 and GFIMPA6; the processes from shear band formation to failure of the two materials are very similar, and again, the evident adiabatic shear band failure happened at larger strain for GFIMPA6. It is noted that the yield stresses for GFPA6 and GFIMPA6 in high rate experiments are 235 and 200 MPa, which are close to their strength in quasi-static tests at -60°C (Fig. 4(c)); however, post-yield failure is only seen at high rates. This indicates that the failure is mainly attributable to the adiabatic shear band, rather than intrinsic material embrittlement. The impact modifier can move the failure to large strains at high strain rate tests, which is consistent with tests at medium rate in Fig. 7.

4.4.3. In-situ damage characterisation using ultra-fast X-ray phase-contrast imaging

Although insightful in capturing thermo-mechanical processes during medium to high strain rates, the high-speed visible light and the IR images cannot provide information about the internal damage processes. To further investigate this, the GFPA6 was characterised using high-speed X-ray micro-imaging at ESRF beamline ID-19.

Fig. 10(a) shows the measured stress-strain curve – even after smoothing the data are noisier than those presented above because of the smaller specimen (diameter 1 mm). The stress drop occurs at 0.3 true strain, which is higher than the 0.2 in Figs. 8(a) and 9(a); this might be due to the sample size or equipment effects. The setup in this test allows 128 frames to be captured during the $\sim 120 \mu\text{s}$ test duration [23]. A

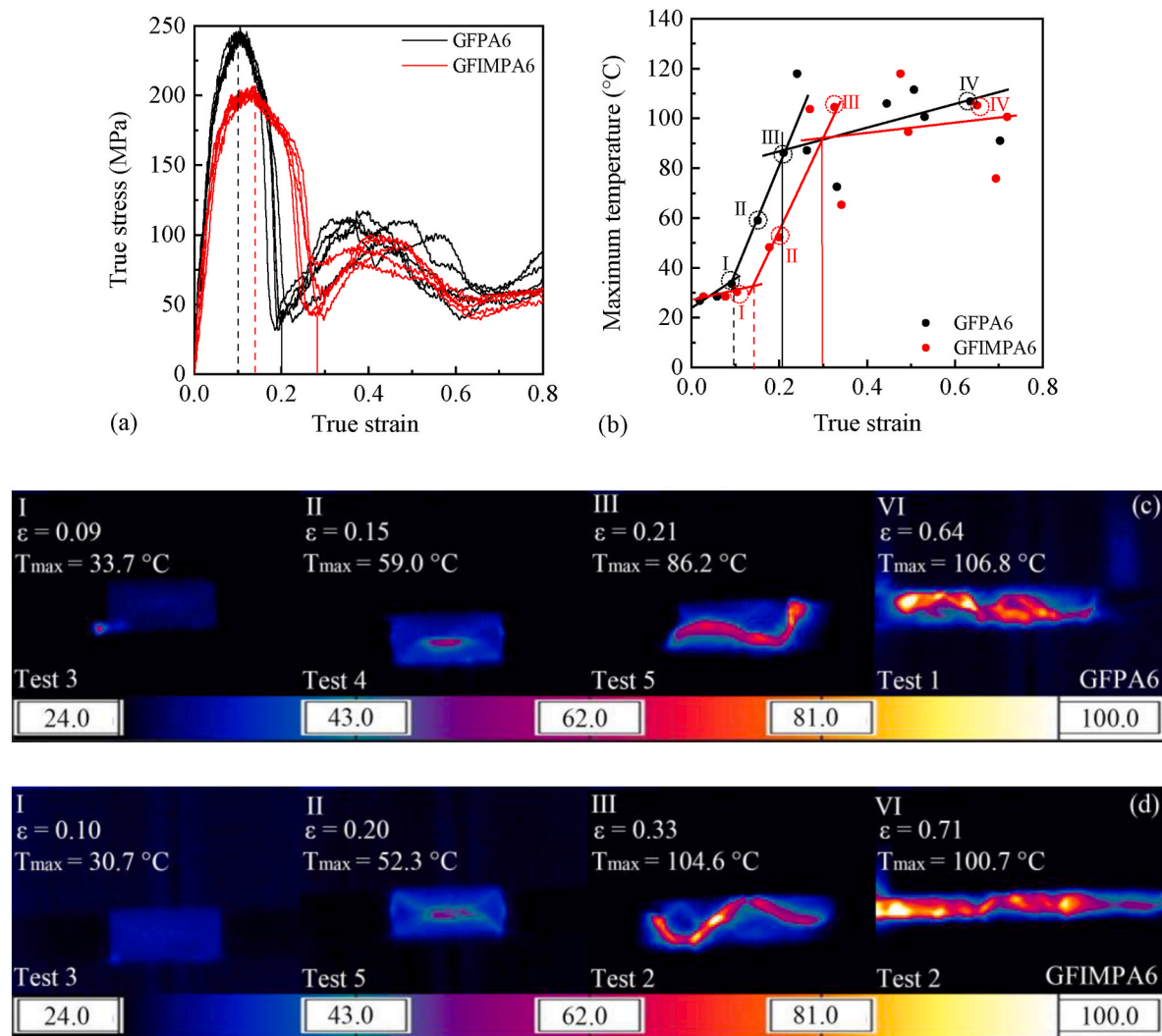


Fig. 9. (a) Stress-strain data from five high strain rate experiments on GFPA6 and GFIMPA6; (b) Maximum temperature rise versus true strain from all the images obtained from these experiments; (c) and (d) Representative thermal images from low to high strain.

number of points were selected and labelled in Fig. 10(a) using red dots, and corresponding phase-contrast images are shown in Fig. 10(b).

In Fig. 10(b), the sample deformation is observed to be inhomogeneous, and the crack is initiated at about 0.25–0.27 true strain. Following that, the crack propagates, accompanied by a significant reduction of sample strength, until the sample fractures. Although the failure timing is different, the failure mode is consistent with the experiments conducted on larger samples in our laboratory.

5. Conclusions

The thermomechanical behaviour of 30 wt% short glass fibre reinforced polyamide 6 (GFPA6) and impact modified glass fibre reinforced polyamide 6 (GFIMPA6) has been characterised over a wide range of temperatures and strain rates. The deformation and failure processes in both materials were investigated using high speed visible, infrared and MHz X-ray phase-contrast imaging. These experimental techniques collectively offer real-time evaluation of surface damage and adiabatic heating, along with monitoring of internal damage progression within the composite specimens. The main contributions of this work are that.

- Both a decrease in temperature and an increase in strain rate increase the strength and stiffness of the PA6 composites, and a bilinear

increase in rate-dependent tests is attributed to the secondary transition of the matrix material.

- Comparing the quasi-static low temperature and dynamic compression tests, the failure of these two composites is a rate-dependent adiabatic shear failure, and the impact-modifier leads the composites to fail at larger strains.
- At medium and high strain rates, the mechanical behaviours and thermal images are well correlated, and there are three stages: small temperature rise before yield, then rapid temperature rise during shear band formation to failure, and finally, a constant temperature after sample fragmentation.
- High-speed X-ray phase-contrast images can provide information about internal damage, which is consistent with the optical and IR observations.
- Advanced high-speed imaging techniques provide new solutions to characterise the deformation and failure of the composite materials, and their combination gives a comprehensive dataset of materials under different loading conditions that can help build a deep mechanistic understanding of advanced materials used in different engineering applications.

CRediT authorship contribution statement

Peihao Song: Writing – original draft, Methodology, Investigation,

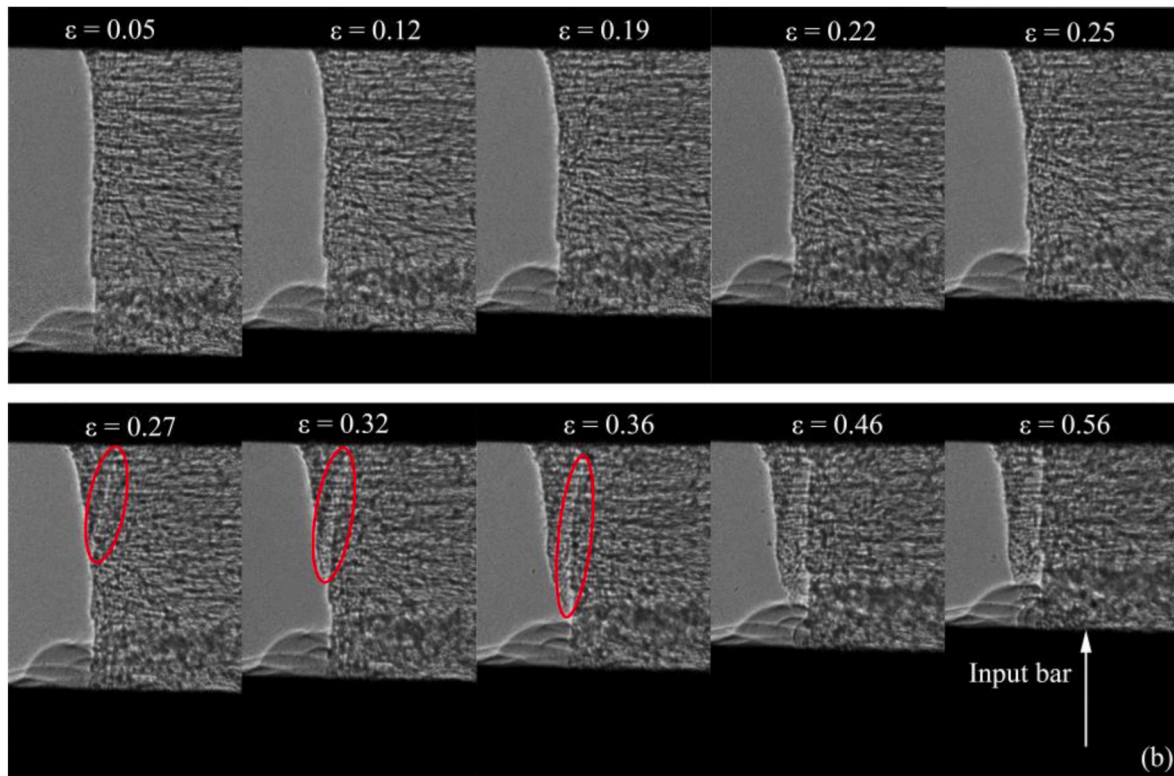
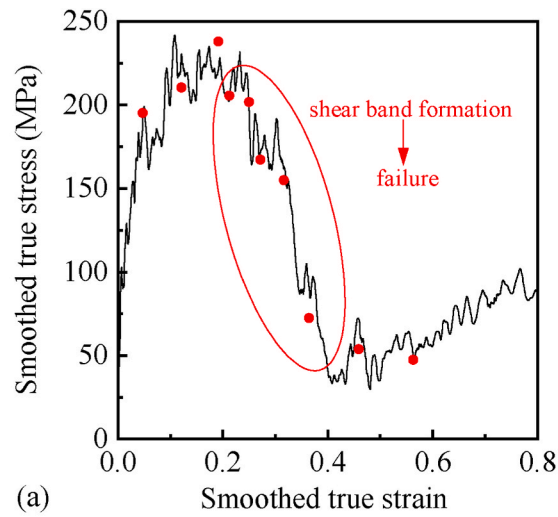


Fig. 10. (a) Smoothed true stress versus train strain curve for GFPA6 tested using the SHPB at ESRF (b) Representative in-situ X-ray phase contrast images at strains indicated by the red circles in (a). (For interpretation of the references to colour in this figure legend, the reader is referred to the Web version of this article.)

Formal analysis, Conceptualization. **Akash R. Trivedi:** Methodology, Investigation. **David J. Chapman:** Writing – review & editing, Methodology, Investigation. **Aaron Graham:** Formal analysis. **Nicholas Hawkins:** Investigation, Data curation. **Bratislav Lukić:** Methodology, Data curation. **Alexander Rack:** Methodology, Data curation. **Clive R. Siviour:** Writing – review & editing, Supervision, Project administration, Funding acquisition, Conceptualization.

Declaration of competing interest

The authors declare that they have no known competing financial interests or personal relationships that could have appeared to influence

the work reported in this paper.

Data availability

All data supporting this study are openly available from the Oxford University Research Archive with DOI [10.5287/ora-dokx1vwzj](https://doi.org/10.5287/ora-dokx1vwzj).

Acknowledgements

This research forms part of the research programme of DPI, project 827t19, *Impact Modelling of Polymers: high-Rate Experiments for Solid-state Simulations*. The authors thank our industrial partner DSM Engineering

Materials for supporting materials in this project, and we also thank Dr Lucien Douven and Dr Tom Engels for their valuable suggestions. We gratefully acknowledge our colleagues on this project, Dr Davide De Focatiis and Grace Owen at the University of Nottingham for their helpful discussions. We also thank the technicians of the Solid Mechanics Group workshop for the manufacture of specimens. We thank the Hypersonics Research Group for the use of the high speed thermal imaging camera, and thank EPSRC for support of thermomechanical

characterisation as part of EP/V003321/1. X-ray imaging was performed at ESRF under proposal beamtime MI-1397, under the Shock BAG supported by the European Union's Horizon 2020 research and innovation program under Grant Agreement No. 870313, Streamline). B.L. acknowledges the support from EPSRC (EP/W003333/1). For the purpose of Open Access, the authors have applied a CC BY public copyright license to any Author Accepted Manuscript (AAM) version arising from this submission.

Appendix A. Material information [25,26]

Table A
Mechanical properties of GFPA6 and GFIMPA6 at dry condition

Mechanical properties	GFPA6	GFIMPA6	Test method
Tensile modulus, MPa	9700	8700	ISO-527-1/-2
Strain at break, %	3.8	5	ISO-527-1/-2
Charpy impact strength (23 °C), kJ/m ²	95	95	ISO 179/1eU
Charpy impact strength (−30 °C), kJ/m ²	75	100	ISO 179/1eU
Charpy notched impact strength (−30 °C), kJ/m ²	14	23	ISO 179/1eA
Charpy notched impact strength (23 °C), kJ/m ²	11	15	ISO 179/1eA

Appendix B. SHPB experiments for GFIMPA6

Static force equilibrium at the 2 bar-specimen interfaces should be checked [18], to confirm that

$$F_T = F_I + F_R \quad (B1)$$

F_I and F_R are the incident and reflected forces; the transmitted force is F_T . Fig. B1(a) shows the stress pulses recorded in the bars, and Fig. B1(b) demonstrates a comparison of the two forces. Finally, the strain rate is shown in Fig. B1(c).

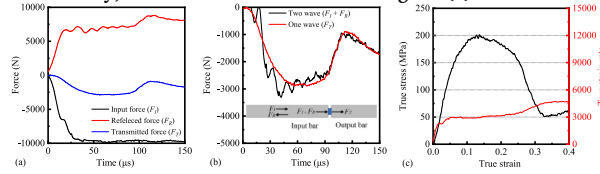


Fig. B1. (a) Force-time curves for an SHPB experiment at about 3000 s^{−1} (b) Forces calculated from one-wave and two-wave analyses (c) True stress-true strain and true strain rate-true stress curves.

Appendix C. Validation of high speed thermal imaging technique [1]

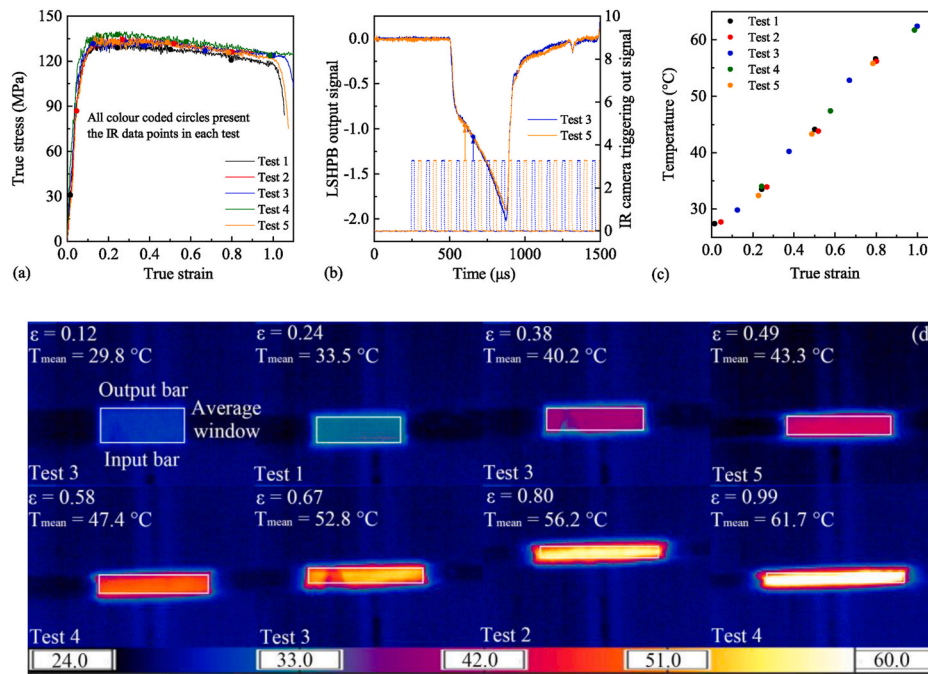


Fig. C1. (a) True stress versus true strain curves for five SHPB experiments on PA6 at about 3000 s^{-1} (b) Time-shifted IR camera triggering out signal and SHPB output bar signal from two experiments (c) Mean temperature versus true strain for all the images obtained from five tests (d) Representative thermal images from low to high strain. Reproduced from Ref. [1].

References

- [1] Song P, Trivedi A, Hawkins N, Graham A, Chapman D, Siviour CR. Thermomechanical characterisation of polyamide 6 over a wide range of rates and temperatures. *Polymer* 2024;300:126907.
- [2] Neis PD, Ferreira NF, Poletto JC, Sukumaran J, Andó M, Zhang Y. Tribological behavior of polyamide-6 plastics and their potential use in industrial applications. *Wear* 2017;376–377:1391–8.
- [3] Fu S-Y, Lauke B, Mai YW. Science and engineering of short fibre-reinforced polymer composites. Woodhead Publishing; 2019.
- [4] Mortazavian S, Fatemi A. Effects of fiber orientation and anisotropy on tensile strength and elastic modulus of short fiber reinforced polymer composites. *Compos B Eng* 2015;72:116–29.
- [5] Parodi E, Govaert LE, Peters GWM. Glass transition temperature versus structure of polyamide 6: a flash-DSC study. *Thermochim Acta* 2017;657:110–22.
- [6] Parodi E, Peters GWM, Govaert LE. Prediction of plasticity-controlled failure in polyamide 6: influence of temperature and relative humidity. *J Appl Polym Sci* 2018;135(11):45942.
- [7] Walley SM, Field JE, Pope PH, Safford NA. A study of the rapid deformation behaviour of a range of polymers. *Phil Trans Roy Soc Lond Math Phys Sci* 1989;328 (1597):1–33.
- [8] Hao P, Laheri V, Dai Z, Gilbert FA. A rate-dependent constitutive model predicting the double yield phenomenon, self-heating and thermal softening in semi-crystalline polymers. *Int J Plast* 2022;153:103233.
- [9] Wang Z, Zhou Y, Mallick PK. Effects of temperature and strain rate on the tensile behavior of short fiber reinforced polyamide-6. *Polym Compos* 2002;23(5):858–71.
- [10] Holmström PH, Hopperstad OS, Clausen AH. Anisotropic tensile behaviour of short glass-fibre reinforced polyamide-6. *Composites Part C: Open Access* 2020;2: 100019.
- [11] Bernasconi A, Cosmi F. Analysis of the dependence of the tensile behaviour of a short fibre reinforced polyamide upon fibre volume fraction, length and orientation. *Procedia Eng* 2011;10:2129–34.
- [12] Karsli NG, Aytac A. Tensile and thermomechanical properties of short carbon fiber reinforced polyamide 6 composites. *Compos B Eng* 2013;51:270–5.
- [13] Bader MG, Collins JF. The effect of fibre-interface and processing variables on the mechanical properties of glass-fibre filled nylon 6. *Fibre Sci Technol* 1983;18(3): 217–31.
- [14] Massaq A, Rusinek A, Klosak M, Bahi S, Arias A. Strain rate effect on the mechanical behavior of polyamide composites under compression loading. *Compos Struct* 2019;214:114–22.
- [15] Río TG-d, Ruiz A. High strain rate mechanical behavior of polyamide 66 and polyamide 66-glass fiber reinforced. *Mech Compos Mater* 2024;59(6):1217–22.
- [16] Wang K, Xiang J, Wang J, Xie G, Liu Y, Peng Y, et al. Effects of printing direction on quasi-static and dynamic compressive behavior of 3D printed short fiber reinforced polyamide-based composites. *Polym Adv Technol* 2022;33(8):2404–15.
- [17] Zeybek MK, Güden M, Taşdemirci A. The effect of strain rate on the compression behavior of additively manufactured short carbon fiber-reinforced polyamide composites with different layer heights, infill patterns, and built angles. *J Mater Eng Perform* 2023;32(24):11050–63.
- [18] Siviour CR, Jordan JL. High strain rate Mechanics of polymers: a review. *J Dyn Behav Mater* 2016;2(1):15–32.
- [19] Song P, Trivedi AR, Siviour CR. Mechanical response of four polycarbonates at a wide range of strain rates and temperatures. *Polym Test* 2023;121:107986.
- [20] Rittel D. On the conversion of plastic work to heat during high strain rate deformation of glassy polymers. *Mech Mater* 1999;31(2):131–9.
- [21] Trivedi AR, Song P, Siviour CR. Experimentally simulating adiabatic behaviour: capturing the high strain rate compressive response of polymers using low strain rate experiments with programmed temperature profiles. *Polym Test* 2022;116: 107773.
- [22] Dodd B, Bai Y. Adiabatic shear localization: frontiers and advances. Elsevier; 2012.
- [23] Song P, Chapman DJ, Graham AM, Lukić B, Rack A, Siviour CR. Thermomechanical characterisation of a thermoplastic polymer and its short glass fibre reinforced composite: influence of fibre, fibre orientation, strain rates and temperatures. *Compos Appl Sci Manuf* 2024;180:108099.
- [24] Sun X, Sory D, Liu K, Lukić B, Simonian D, Wong KL, et al. Effect of temperature on high strain-rate damage evolving in CFRP studied by synchrotron-based MHz X-ray phase contrast imaging. *Compos B Eng* 2024;279:111445.
- [25] DSM. Akulon® K224-G6 data sheet. 2023.
- [26] DSM. Akulon® K224-PG6 data sheet. 2023.
- [27] Ghanta TS, Aparna S, Verma N, Purnima D. Review on nano- and microfiller-based polyamide 6 hybrid composite: effect on mechanical properties and morphology. *Polym Eng Sci* 2020;60(8):1717–59.
- [28] Plastics. Determination of tensile properties. Part 1, General principles. London: British Standards Institution; 2019.
- [29] Trautmann A, Siviour CR, Walley SM, Field JE. Lubrication of polycarbonate at cryogenic temperatures in the split Hopkinson pressure bar. *Int J Impact Eng* 2005; 31(5):523–44.
- [30] Cohen A, Levi-Hevroni D, Fridman P, Chapman D, Rack A, Olbinado MP, et al. In-situ radiography of a split-Hopkinson bar dynamically loaded materials. *J Instrum* 2019;14(6):T06008.
- [31] Wilkins SW, Gureyev TE, Gao D, Pogany A, Stevenson AW. Phase-contrast imaging using polychromatic hard X-rays. *Nature* 1996;384(6607):335–8.
- [32] Mulliken AD, Boyce MC. Mechanics of the rate-dependent elastic-plastic deformation of glassy polymers from low to high strain rates. *Int J Solid Struct* 2006;43(5):1331–56.
- [33] Menard KP, Menard NR. Dynamic mechanical analysis in the analysis of polymers and rubbers. *Encycl Polym Sci Technol* 2002:1–33.